Toward objective rockfall trajectory simulation using a stochastic impact model

Franck Bourrier, L. Dorren, François Nicot, F. Berger, F. Darve

Toward objective rockfall trajectory simulation using a stochastic impact model

Franck Bourrier [a*], Luuk Dorren [b], François Nicot [a], Frédéric Berger [a] and Félix Darve [c]

a Cemagref - 2, rue de la Papeterie - BP 76 - 38 402 Saint Martin d'Hères Cedex – France

b Federal Office for the Environment FOEN - Hazard Prevention Division - 3003 Bern - Switzerland

c L3S-R - INPG, UJF, CNRS - Domaine Universitaire - BP 53 - 38 041 Grenoble Cedex 9 - France

**Corresponding author. Tel.: +33 4 76 76 27 27; Fax: +33 4 76 51 38 03; E-mail: franck.bourrier@cemagref.fr.*

Abstract:

The accuracy of rockfall trajectory simulations depends to a large extent on the calculation of the rebound of falling boulders on different parts of a slope where rockfalls could occur. The models commonly used for rebound calculation are based on restitution coefficients, which can only be calibrated subjectively in the field. To come up with a robust and objective procedure for rebound calculation, a stochastic impact model associated with an objective field data collection method was developed and tested in this study. The aims of this work were to assess the adequacy of this approach and to evaluate the minimum amount of field data required to obtain simulation results with a satisfactory level of predictability. To achieve these objectives, the rebound calculation procedure developed was integrated into a three-dimensional rockfall simulation model, and the simulated results were compared with those obtained from field rockfall experiments. For rocky slopes, the simulations satisfactorily predict the experimental results. This approach is advantageous because it combines precise modelling of the mechanisms involved in the rebound and of their related variability with an objective field data collection procedure which basically only requires collecting the mean size of soil rocks. The approach proposed in this study therefore constitutes an excellent basis for the objective probabilistic assessment of rockfall hazard.

Keywords: 3D simulations; field experiments; restitution coefficients; rockfall rebound; stochastic modelling; Rockyfor3D.

1. Introduction

As shown by the recent accidents occurring in March 2006 in the French Alps and June 2006 on the Gotthard highway in Switzerland, rockfall is one of the main natural hazards that pose risks to residential areas, infrastructures, and populations in the Alps. Rockfall is generally defined as the removal of individual boulders from a cliff face (Varnes, 1978; Whalley, 1984; Selby, 1993; Cruden and Varnes, 1996). This study focuses on single falling rocks with a volume up to 1.3 m^3. In rockfall hazard assessment, trajectory simulation models are increasingly used for designing protective measures such as nets and dams (Descoeudres, 1997; Peila et al., 1998; Nicot et al., 2001, 2007) or for making hazard maps (Kobayashi et al., 1990; Evans and Hungr, 1993; Guzzetti et al., 2002; Chau et al., 2004; Jaboyedoff et al., 2005; Bourrier et al., 2008b; Frattini et al., 2008).

The most difficult process to simulate in such trajectory models is the rebound, which describes the impact of the falling boulder on the slope surface. To calculate such a rebound, a wide range of algorithms is currently available, which are summarised in Guzzetti et al. (2002), Dorren (2003), and Heidenreich (2004). Rebound deterministic modelling remains highly speculative since the information available on the mechanical and geometrical properties of the soil is not sufficient to perform a relevant deterministic prediction of boulder rebound. In particular, the characterisation of the spatial distributions of the parameters required for rebound calculation generally result from a field survey which, for practical reasons, cannot be exhaustive. Stochastic approaches have therefore been proposed (Paronuzzi, 1989; Pfeiffer and Bowen, 1989; Azzoni et al., 1995; Dudt and Heidenreich, 2001; Guzzetti et al., 2002; Agliardi and Crosta, 2003; Jaboyedoff et al., 2005; Bourrier et al., 2007, 2008b; Frattini et al., 2008) to account for the variability of the rebound. Most of these approaches are based on two parameters, both called restitution coefficients, which proved to partially represent the complexity of the rebound (Wu,

1985; Bozzolo and Pamini, 1986; Chau et al., 1998; Ushiro et al., 2000; Chau et al., 2002; Heidenreich, 2004). The problem is that stochastic variation of the restitution coefficients only account for the variability related to terrain characteristics. Variability due to the kinematics of the falling boulder is not accounted for. In addition, estimating the values of these two parameters in the field is a difficult task mainly based on literature values that are associated with certain surface characteristics of the slope. Overviews of commonly used values for restitution coefficients are given in (Paronuzzi, 1989; Pfeiffer and Bowen, 1989; Azzoni et al., 1992; Azzoni and De Freitas, 1995; Chau et al., 2002; Agliardi and Crosta, 2003; Scioldo, 2006). Most models are very sensitive to the values of these restitution coefficients. In addition, the values in the literature vary significantly for identical surface characteristics. The resulting subjectivity in the choice of these parameter values therefore partly explains the large variation in the results obtained when applying different models, or even the same model used by different operators, at the same site (Interreg IIc, 2001; Berger and Dorren, 2006).

To overcome these difficulties, a more objective rebound calculation procedure based on a stochastic impact model was developed. This procedure models the variability associated with the rebound and only requires collecting a very limited set of field parameters: the size of the falling boulder and the sizes characterising the rocks composing the slope surface. Our first objective was to test and validate the procedure developed. The second objective was to evaluate the minimum amount of field data required to obtain simulation results with a satisfactory level of predictability.

This paper first explains the rebound calculation procedure developed and its integration into a three-dimensional rockfall trajectory simulation model. Then the simulation results are compared with those obtained from field rockfall experiments and discussed.

2. Full-scale rockfall experiments on a mountain slope

Full-scale rockfall experiments were carried out in an avalanche track in the Forêt Communale de Vaujany in France (N. 45°12′, E. 6°3′). The study area covers an Alpine slope ranging from 1200 to 1400 m above sea level with a mean gradient of 38°. The experimental site is part of a hillslope that is formed

by a postglacial talus slope (Fig. 1), downslope from rock faces consisting of the “Granite des Sept Laux”, which belong to the crystalline Belledonne massif. The talus cone mainly consists of rock avalanche, snow avalanche, and rockfall deposits. The study site is ~ 100 m wide and 570 m long (distance between the starting point and the lower forest road, measured along the slope). Between the starting point and the lower forest road, it has the shape of a channel with a maximum depth and width of 2 and 10 m, respectively. Since avalanches occur every year in this channel, it is denuded of trees.

Fig. 1.

The protocol was identical for all rockfall experiments. Before each boulder release, the volume of the boulder was measured and the boulder was coloured with biodegradable paint so that it left traces after rebounding on the slope. The volume was estimated by measuring the height, width, and depth along the three most dominant boulder axes and by assuming that the boulders were rectangular. A total of 100 boulders were released individually, one after the other. The mean volume was 0.8 m^3, and the standard deviation 0.15 m^3 (Fig. 2).

Fig. 2.

A front shovel was used to release the boulders down the slope, starting with a free fall of 5 m. As soon as the boulder stopped, the impact locations and stopping points were captured with an Impulse LR 200 laser distance meter manufactured by Laser Technology, Inc. (Centennial, CO, USA). In addition, the rockfall trajectories were filmed by five digital cameras, which were placed so that the camera planes were perpendicular to the channel, which is the preferred rockfall path, and 30 m away (Fig. 1). The cameras were fixed at a height of 10 m in trees. Additional details on the experiments are given in Dorren et al. (2006).

The digital films of the 100 rockfall trajectories were analysed using image processing software called AviStep 2.1.1 (developed by M. Delabaere, St. Denis de la Réunion, France). This program extracts the position and the velocity of a moving particle for each individual image in a digital film using the following principle. First, in the first image of each film, the field-measured rebound distances are identified. Second, soil surface detection is conducted by linking the successive impact points in the films assuming that soil surface is linear between two impact points. Third, the two-dimensional trajectory of each falling boulder was analysed using a sequence of movie images (Fig. 3). Finally, the analysis of the movie images provided the rebound heights, i.e., the maximum vertical distance between the centre of the boulder and the slope's surface, as well as the position of the boulder for every image (every 0.04 s). This makes it possible to determine the velocity.

Since the resolution of the movie images did not allow for a precise measurement of the rotational velocity, only the translational kinetic energy E_{trans} was calculated to reduce the uncertainty in the results. The translational kinetic energy E_{trans} of a falling boulder is calculated as:

$$E_{trans} = \frac{1}{2} m_b V^2 \qquad (1)$$

where m_b is the mass, and V is the translational velocity of the boulder.

The experimental results therefore do not provide information on either the rotational kinetic energy E_{rot} or the total kinetic energy E_{tot}, which are defined as follows:

$$E_{rot} = \frac{1}{2} I_b \omega^2 \qquad (2)$$

and

$$E_{tot} = E_{trans} + E_{rot} \qquad (3)$$

where I_b is the moment of inertia, and ω is the rotational velocity of the boulder.

Fig. 3.

3. Trajectory simulation using a stochastic rebound algorithm

The simulation model used is the 3D rockfall trajectory model Rockyfor3D, which has been developed since 1998 (Dorren et al., 2006). This model simulates the rockfall trajectory in 3D by calculating sequences of parabolic free fall through the air and rebounds on the slope, as well as impacts against trees, if specified. Rolling is represented by a sequence of short-distance rebounds and sliding is not modelled. Falling boulders are represented in the model by spheres using a hybrid approach. This means that, during parabolic free fall, the falling sphere is represented by a single point (lumped mass) and, during the rebound calculation, by a real sphere. The three major components of Rockyfor3D are 1) the parabolic free fall calculation and its intersection with the topography, 2) the rebound calculation, and 3) the fall direction calculation after rebound.

3.1. Parabolic free fall

The parabolic free fall is calculated with a standard algorithm for a uniformly accelerated parabolic movement through the air. This calculation determines the position and the normal (with respect to the local slope) V_n^{in}, tangential V_t^{in}, and rotational ω^{in} velocities at the intersection with the slope topography, represented by a Digital Elevation Model (DEM). As such, Rockyfor3D simulates a 3D trajectory by calculating the displacement of the boulder position along the *x*-, *y*-, and *z*-axes (Fig. 4). Here, the *z*-axis corresponds to its vertical position, the *x*-axis to the east–west direction, and the *y*-axis to the north–south direction (Fig. 4A). By its *x* and *y* coordinates, the 3D trajectory is linked to a set of raster maps with a resolution between 1 and roughly 20 m. For this study, however, the raster resolution was 2.5 m. The raster maps provide information on the topography (DEM), the slope surface characteristics, and the release points (for this study, only one release raster cell was defined).

Knowing the position of the rebound and the slope surface characteristics defined by the raster maps at this position, as well as the velocities before rebound, the rebound calculation using the stochastic impact model can be initiated.

Fig. 4.

3.2. Stochastic impact model

The rebound calculation determines the normal V_n^{out}, tangential V_t^{out}, and rotational ω^{out} velocities after rebound based on the velocities before rebound, called incident velocities, and on the parameters determining the energy loss during the rebound. The rebound model initially integrated in Rockyfor3D (Dorren et al., 2006) was replaced by a stochastic impact model that calculates the velocity vector after rebound $\boldsymbol{V}^{out}$ from the velocity vector before rebound $\boldsymbol{V}^{in}$ following the expression:

$$\mathbf{V}^{out} = \mathbf{A}\mathbf{V}^{in} \text{ with } \mathbf{V}^{out} = \begin{bmatrix} V_t^{out} \\ V_n^{out} \\ \omega^{out} \end{bmatrix}, \ \mathbf{A} = \begin{bmatrix} a_1 & a_2 & a_3 \\ a_4 & a_5 & a_6 \\ a_7 & a_8 & a_9 \end{bmatrix}, \ \mathbf{V}^{in} = \begin{bmatrix} V_t^{in} \\ V_n^{in} \\ \omega^{in} \end{bmatrix} \quad (4)$$

This means that each of the three velocities after rebound (V_t^{out}, V_n^{out}, and ω^{out}) is calculated with the three incident velocity components (V_t^{in}, V_n^{in}, and ω^{in}) and three coefficients of matrix **A**.

For example, the tangential component of the velocity after rebound V_t^{out} is expressed as follows:

$$V_t^{out} = a_1 V_t^{in} + a_2 V_n^{in} + a_3 \omega^{in} \quad (5)$$

The coefficients a_i, as well as the correlations between them, are characterised by normal probability distribution functions. These allow the model to account for the high variability of the local slope surface characteristics and the kinematics of the rebounding sphere. Specific information can be found in Bourrier et al. (2007, 2008b).

Fig. 5.

Because of the defined inter-relationships between the outgoing and incident velocity components, the stochastic impact model differs completely from classical rebound algorithms. Most of these only use a tangential R_t and a normal R_n restitution coefficient for different slope surface types (see Guzzetti et al.,

2002; Dorren, 2003), which are defined by the user but are not related to all three incident velocity components. Many authors have already revealed that this approach introduces errors in rebound calculations. The R_t and R_n coefficients are defined as follows:

$$R_t = \frac{V_t^{out}}{V_t^{in}} \quad (6)$$

$$R_n = -\frac{V_n^{out}}{V_n^{in}} \quad (7)$$

Contrary to classical models, the restitution coefficients R_t and R_n that can be recalculated from the velocities before and after rebound as predicted by the stochastic impact model are not constant values. They both depend on all the incident kinematic parameters and the terrain characteristics. Figure 6 shows an example of the effect of the incident angle on the mean restitution coefficients R_t and R_n predicted by the stochastic impact model.

Fig. 6.

The values of the coefficients a_i defined in matrix **A** are derived from the statistical analyses of a large data set obtained from numerical simulations of impacts (Bourrier et al., 2007, 2008a, 2008b). These numerical simulations of impacts were previously calibrated from laboratory experiments of the impact of a 10-cm spherical rock on a coarse soil composed of gravels ranging from 1 cm to 5 cm (Bourrier et al., 2008b). The adequate agreement between the laboratory experiments and the numerical simulations of impacts proves that the impact simulations, and consequently the stochastic impact model, satisfactorily express the energy transfers occurring during the impact of a boulder on a coarse soil. Although the calibration of the numerical model of impacts was satisfactory, one limitation could stem from the differences in the size of the impacting and soil rocks during calibration and during application in this study. However, the influence of the scale change effects was proved to be small by comparing the results of the numerical simulations of impacts at different scales (Bourrier, 2008).

197 For this study, the parameters of the stochastic impact model were determined for five fixed ratios, which
198 have the values 1, 2, 3, 4, and 5, between the radius of the falling boulder R_b and the mean radius of the
199 particles constituting the slope surface R_m. For each R_b/R_m ratio, a fixed set of model parameters was
200 calculated. For larger ratios, the model has not yet been calibrated, which means that it is currently not
201 suitable for rebounds of large boulders on fine soils.

202 *3.3. Calculation of the fall direction*

203 The fall direction in the *x–y* plane is primarily determined by the slope topography at the rebound position
204 and is calculated by a probabilistic algorithm. During each subsequent rebound, the model allows the
205 sphere to deviate from its direction before rebound towards the direction of the aspect of the raster cell in
206 which the boulder rebounds (Figs. 5 and 7). The aspect is the downslope direction of the maximum rate of
207 change in value from each cell in a raster to its neighbouring ones and represents the steepest slope
208 direction. The deviation angle δ (Fig. 5) is determined by a random number that defines whether the
209 boulder is deviated between 0 and 22.5º from its original direction, or 22.5–45º, or 45–50º. The first case
210 has a 72% probability of occurrence, the second one has a 24% probability, and the third one a 4%
211 probability (Fig. 7). These deviation angles and their related probabilities are based on the experimental
212 results presented in Dorren et al. (2005). If the sphere moves upslope, a maximum deviation of 22.5° is
213 allowed for both directions lateral to the direction before rebound. If the boulder enters a depression in the
214 DEM, the direction before and after rebound remains unchanged.
215
216 Fig. 7.
217

218 *3.4. Input data*

219 The DEM used for the experimental site covers an area from the release point to the opposite river bank
220 in the valley bottom. The DEM was created using inverse distance-weighted interpolation (see for

instance Weber and Englund, 1992) of, on average, three *x*, *y*, *z* points per DEM cell. These points were collected in the field with a detailed topographical survey using a laser distance meter and a compass. The topographical survey was conducted so that a mean density of 1 point/m was available in all directions. We created this DEM because, due to the surrounding forest cover, GPS measurements are not accurate on the study site and a high-resolution, photogrammetric or LiDAR-derived DEM was not available. Verification with an available 10-m DEM and an orthophoto showed that the accuracy of the created DEM was about 1 m in the *x*–*y* plane and 0.5–1.5 m in the *z*-direction.

At the release point, boulders were dropped from a height of 5 m. The simulated boulders were assumed to be spherical, and the distribution of their volumes was identical to the experimental distribution (Fig. 2). The errors associated with volume estimation were therefore the same in the experiments and in the simulations. Volume estimation errors were reduced as much as possible by choosing the released boulders in a quarry so that they were as spherical as possible.

The slope surface characteristics were determined in the field by identifying homogenous zones that are represented as polygons on a map (Fig. 1). Each polygon defines the size of the material covering the slope. To represent the size of the surface material in this polygon map, we used two different approaches. The first one, which is called method A ("size classes"), describes the surface with three size probability classes according to Dorren et al. (2006). The second one, called method B ("mean size"), is a more simplified description, which is based only on the mean radius R_m of the material covering the slope. Method A aims at giving a precise description of the size of the surface material and its variation. The method uses three roughness classes Rg_{70}, Rg_{20}, and Rg_{10}. These classes represent the diameter of the obstacle, corresponding to rocks covering the soil surface, encountered by a falling boulder during 70%, 20%, and 10%, respectively, of the rebounds in a homogenous zone. For method A, the field survey therefore consists of estimating the equivalent diameter of the rocks covering the soil surface corresponding to the three classes Rg_{70}, Rg_{20}, and Rg_{10} in each homogenous zone on the study slope. During each rebound calculation, the mean radius R_m of the material encountered by the impacting boulder was randomly chosen from the three material size values Rg_{70}, Rg_{20}, and Rg_{10} given their

247 accompanying probabilities. In method B, only one mean radius R_m value represented the material size in
248 each homogenous zone. Rebound was therefore calculated by considering R_m the mean radius of the rock
249 encountered by the falling boulder in a given zone.
250 In the rebound model used, the value of the R_b/R_m ratio is rounded to the nearest integer with a maximum
251 of 5. A set of rebound model parameters (a_i coefficients) was determined depending on the value of the
252 R_b/R_m ratio. Table 1 reports the values used for all the polygons defined and shown on the map in Fig. 1.
253
254 Table 1.
255

256 *3.5. Simulation scenarios*

257 Rockfall trajectory simulations were carried out using method A ("size classes") and method B ("mean
258 size"). For each method, 100, 1000, 2000, 5000, and 10000 falling boulders were simulated. For each set
259 of simulations, the probability distribution functions of the velocity, translational kinetic energy, and
260 passing height were compared with the corresponding experimental distributions at two "evaluation lines"
261 (Figure 1). Evaluation line 1 (EL1) was located 185 m from the starting point, measured along the slope,
262 directly in the centre of the viewing plane of camera 4. Evaluation line 2 (EL2) was located after 235 m,
263 in the centre of the viewing plane of camera 5. In addition, the spatial patterns of the trajectories, the
264 passing frequencies per raster cell, and the stopping locations of the simulated boulders were analysed.
265 The latter were compared with stopping locations observed during the field rockfall experiments.

266 *3.6. Rebound analysis*

267 If the agreement between the experimental and simulated results is satisfactory, the simulations can
268 collect additional information on the kinematics of the falling boulders, which cannot be measured during
269 the full-scale field experiments. First, precise values of the rotational kinetic energy of the falling
270 boulders at EL1 and EL2 can be obtained from simulations, whereas the rotation of the falling boulder

cannot be precisely measured from the experimental films. In the simulations, the rotational kinetic energy of the falling boulder E_{rot} can therefore be compared with the translational kinetic energy of the falling boulder E_{trans} and with the total kinetic energy of the falling boulder E_{tot}.

Information regarding the incident kinetic energy for all rebounds can also be collected, whereas this is not possible from field experiments. In particular, for each rebound, the simulations provide information on the distribution of the incident kinetic energy between the tangential, normal, and rotational incident velocity components. Starting from Eqs. 1, 2, and 3, the incident kinetic energy E_{tot}^{in} is divided into normal incident energy E_{n}^{in}, tangential incident energy E_{t}^{in}, and rotational incident energy E_{rot}^{in} defined as follows:

$$E_{tot}^{in} = E_{t}^{in} + E_{n}^{in} + E_{rot}^{in} \quad (8)$$

$$E_{t}^{in} = \frac{1}{2} m_b (V_t^{in})^2 \quad (9)$$

$$E_{n}^{in} = \frac{1}{2} m_b (V_n^{in})^2 \quad (10)$$

$$E_{rot}^{in} = \frac{1}{2} I_b (\omega^{in})^2 \quad (11)$$

Finally, to compare the implemented rebound algorithm to classical rebound models based on the use of restitution coefficients, the R_t and R_n values obtained during the simulations were computed using the classical definition given in Eqs. 6 and 7.

4. Results

1000 rockfall simulations were required to provide stable predictions, meaning that the variation in the means and standard deviations of the parameters measured on EL1 and EL2 became < 5%. However, to decrease the variation in the results as much as possible, 10000 simulations were executed for both methods.

4.1. Kinematic results at the evaluation lines

The comparisons between the experimental and simulated results at EL1 and EL2 show that both the mean values and standard deviations were predicted accurately for boulder velocity, passing heights, and translational kinetic energy (Table 2). However, in most cases, the simulated mean values and standard deviations were slightly smaller than the experimental values. In addition, the predictions obtained using method B ("mean size") were systematically closer to the experimental results than those obtained using method A ("size classes"). All relative errors (RE) (Table 3) are < 21% for method B, whereas they reach up to 32% for method A.

The shapes of the distributions of the simulated quantities were very similar for methods A and B (Fig. 8). These distributions were also similar to those obtained from the experimental results. On the contrary, the maximum values were overestimated by the simulations, irrespective of the method used (Table 3).

The statistical Kolmogorov-Smirnov test was performed to compare all the simulated distributions with the corresponding experimental distributions. If the result of the test is 0, it can be assumed that the simulated and experimental results are similar. If the result is 1, this is not the case. The similarity hypothesis is rejected if the p-value associated with the test is less than 0.05. The larger the p-value is, the more plausible the hypothesis that the two samples belong to the same distribution. The results of the Kolmogorov-Smirnov tests showed that method B ("mean size") provided a better prediction of the experimental distributions because the similarity hypothesis was only rejected once out of 6 comparisons. For method A ("size classes"), it was rejected 4 times out of 6 comparisons. In addition, the p-value obtained when comparing the simulated distributions to the measured distributions were all between 0.01 and 0.3 whatever method was used, which means that the simulated distributions were not significantly different from the experimental distributions. Both methods A and B can therefore be considered suitable to simulate the experimental results.

Table 2.

Table 3.

Table 4.

Fig. 8.

4.2. Rockfall trajectories

The numbers of boulders deposited with decreasing altitude are presented in Fig. 9, for both the experimental and simulated results. The simulations, using methods A and B, provided values similar to the experimental values for the distribution of stopping points, especially for boulders reaching low altitudes. Interestingly, predictions using method A ("size classes") resulted in a slight underestimation of the percentage of passing boulders with decreasing altitude. On the contrary, the simulations using method B ("mean size") provided a slight overestimation. For boulders stopping just after the release point and for boulders reaching long distances from the release point (> 350 m), both methods predicted larger percentages of passing boulders than the experimental results.

Fig. 9.

The comparison between simulated run-out zones and experimental stopping points (Fig. 10) showed that, first, the simulated run-out zone was larger than the one observed during the experiments. Second, discrepancies were observed for stopping points located below the forest road. In the experiments, two distinct deposit areas were observed, whereas the simulated passing frequencies only highlighted one of them located on the bottom left of the maps in Fig. 10.

Fig. 10.

4.3. Information gathered from simulations

Since we consider that the agreement between the experimental and simulated results is highly acceptable, we used the simulations to study kinematical parameters that could not be measured in the field, in particular the distribution of the rotational velocity of the falling boulder (Fig. 11). The mean value of the E_{rot}/E_{tot} ratio was 6% for EL1 and 8% for EL2. In addition, the associated standard deviation was 7% for EL1 and 8% for EL2.

Fig. 11.

Further, the simulated E_t^{in} / E_{tot}^{in} ratios (Fig. 12) showed that most of the incident energy was associated with the tangent-to-soil-surface component of the incident velocity. This result was confirmed by the distribution of the incidence angle (Fig. 13), which highlights the small values of this angle. Finally, the simulation results provided information on the distribution of R_t and R_n restitution coefficients for all rebounds, as shown in Fig. 14.

Fig. 12.

Fig. 13.

Fig. 14.

5. Discussion

5.1. Comparison of the experimental and simulation results

The comparisons of the experimental and simulated results, using methods A and B, showed that the 3D trajectory simulation could predict rockfall trajectories and kinematics. Reproducible simulation results were obtained from 1000 simulations onwards, which makes 3D trajectory simulation feasible. However, in this study, there were fewer sources of variability than in the daily practice of rockfall hazard assessment. In particular, the rockfall starting position and the boulder volumes were exactly known. In practice, the latter are not always easy to predict.

The differences between the observed and simulated distributions, the maximum values in particular, could stem from the fact that, in the experiments, the distributions were based on only 100 rockfall experiments. They therefore do not represent the full asymptotic distribution that would have been obtained from a very large number of experiments. However, the global shape of the distribution, such as the most probable value and the global distribution of the values, was satisfactorily represented. Thus, if only the global characteristics of the distributions are compared, the simulated distributions can be considered good predictions, which was confirmed by the results of the Kolmogorov-Smirnov test, in particular for method B ("mean size").

The comparisons between the simulated and the experimental stopping points showed the capability of the rockfall model to predict run-out distances (Fig. 9). However, Fig. 9 shows that method B ("mean size") approached the experimentally observed deposit pattern best. Neither method A nor B reproduced the number of boulders stopping in the upslope section of the test site. These blocks stopped within the first 20–40 m from the release point due to sliding on the side with the largest surface after the first rebound. Figure 9 shows that this accounted for ~ 5% of the released boulders. For large distances from the release point (350 m and farther), the differences between the simulated and the experimental maximum run-out distances (Fig. 9) resulted from the rebound algorithm not being adapted to the surface material consisting of soils composed of fine particles, which was found in the valley bottom (Fig. 10).

The algorithm was specifically developed for rocky surfaces and therefore will not produce realistic results for other soil types.

Although the simulated run-out zones were larger than the experimental run-out zones (Fig. 10), the 1% pass frequency limit, i.e., the limit passed by 1% of the boulders, correspond quite well to the experimentally observed stopping points only (Fig. 10), especially for method B.

The existence of two deposit areas was not reproduced by the simulations. The simulated passing frequency maps show two main trajectory paths upslope of the forest road, which converge into a single path in the downslope section. The experimental trajectories, however, also show two distinct paths in the downslope section. The difference between these experimental and simulated patterns resulted from an imperfect digital representation of the terrain in the DEM south-west of the middle forest road (Fig. 15). This local discrepancy induced slight changes in the pattern of the trajectory path and in the shape of the run-out zone associated with the 1/100 pass frequency (Fig. 10).

Fig. 15.

Finally, the comparison of the results obtained by method A and method B raises questions on how precise the parameter values estimated in the field must be. For methods A and B, the simulated distributions of velocities, rebound heights, and energies (Fig. 8) as well as the run-out zones (Fig. 9) were very similar. The detail of the description of the slope surface characteristics therefore only slightly influences the simulation results. Our experience shows, however, that in the field it is easier to estimate three size classes than a single one, as shown in Fig. 16. For example, on a slope covered with rather fine scree (< 5 cm), quite some rocks measured 10 cm in diameter, and 10% of the surface covered with 20-cm rocks, it is quite difficult to estimate a single, valid, mean particle size. The “size classes” method describes the mean size of the particles that cover 70%, 20%, and 10% of the surface, with 70% = 5 cm, 20% = 10 cm, and 10% = 20 cm. Since method B (“mean size”) provided more accurate results, this

implies that method A (“size classes”) could be used in the field for a better estimate of the single mean particle size, so that method B (“mean size”) could be used in the simulation.

Fig. 16.

5.2. Advantages and limitations of the approach

An advantage of the approach presented here is that simulation can be used to gather information that cannot be obtained in the field (see section 3.6). First, the simulated distributions of the rotational kinetic energies compared to the total kinetic energy at EL1 and EL2 show that the translational velocity of the boulder mainly determines the total boulder kinetic energy (Fig. 11). One could note a slight trend toward a downhill increase in the E_{rot}/E_{tot} ratio, which may be due to the specific topography of the study site. Although the rotational energy was smaller than the translational energy, the knowledge of the distribution between these two energies is essential for designing effective protective structures. The translational kinetic energy mainly determines the design of the structure (structural strength performance), whereas the rotational kinetic energy determines the capability of the structure to prevent boulders from rolling over the structure (structure shape efficiency).

Another advantage of the approach presented is the insight obtained in the commonly used coefficients R_t and R_n. The values of the R_t calculated from the simulated rebounds (Fig. 14) are in accordance with common values for talus slopes, but they show that the variability of R_t is even greater than assumed in the literature. In contrast, the values of the R_n coefficients (Fig. 14) are extremely high compared to the common values, which generally range from 0.25 to 0.65. The dependence of R_t and R_n recalculated from the stochastic impact model on the incidence angle explains this phenomenon (Fig. 6). For small incidence angles, which correspond to most of the rockfall impacts in the simulations (Fig. 13), the values of R_t depend only slightly on the incidence angle; they correspond to common values ($R_t \approx 0.7$; Fig. 14). On the contrary, the values of R_n are very high ($R_n > 1$) compared to common values (Fig. 14). However,

in the case of a vertical impact, the R_n values predicted by the stochastic impact model (Fig. 6) are in accordance with common experimental results ($R_n \approx 0.4$). The main reason for these differences is that the common values of R_n are generally obtained from experimental campaigns conducted for boulders falling vertically on a slope surface. This does not correspond to the simulated impact cases because simulation incidence angles were, for the most part, < 50°, as shown in Fig. 13. The high values of R_n in the simulations explain that, although the incident normal velocity V_n^{in} was small for impacts that were parallel to the slope's surface, the normal velocity of the boulder after a rebound can be very high because of the energy transfer from the rotational to the translational kinetic energy. This phenomenon is not accounted for in classical rebound algorithms, whereas it is included in the stochastic impact model.

The values of R_n should therefore be chosen with caution when performing a rockfall trajectory analysis using classical rebound algorithms. However, the importance of R_n is generally subordinate to R_t. Indeed, properly modelling the transfer of the tangential incident energy between the falling boulder and the soil during a rebound is essential because Fig. 12 shows that the tangential incident energy is, in most cases, determinant for the total incident energy (93% of the calculated E_t^{in} / E_{tot}^{in} ratios are > 0.75).

The two main points of interest in the rebound calculation procedure developed herein are, first, precisely modelling the mechanisms governing the rebound as well as their associated variability and, second, the more objective field data collection procedure. Both points are of great interest for rockfall hazard mapping, which demand a satisfactory prediction of the variability of both the stopping points and the kinematics of the falling boulders. Following the proposed approach, hazard mapping can be greatly improved because it allows the reliable spatial characterisation of the passing frequencies as well as of the mean and standard deviation values of the rockfall energies (intensity). Rockfall hazard mapping approaches based on combinations of intensity and probability, such as those developed in Switzerland (Raetzo et al., 2002; Jaboyedoff et al., 2005), can therefore be used with increased confidence.

However, this work is limited by the partial character of the validation. From a theoretical point of view, the amount of experimental data is not (and almost never is) sufficient to validate simulated rare events.

Since the performance and analysis of 1000 full-scale rockfall experiments would take roughly 10 years, one must rely on simulations to predict extreme events, even though they are not fully validated.

Another limitation of this study is that the stochastic impact model developed can only be used on rocky slopes. However, similar approaches could be developed to characterise the rebound of a boulder on all types of soil provided that large data sets composed of reproducible and precisely defined impact tests are available for statistical analysis. To create these data sets, the direct use of laboratory or field experiments is not suitable. However, they can be generated from numerical simulations that have previously been calibrated using these experiments. That is exactly were the challenge lies.

6. Conclusions

This paper has investigated a newly developed stochastic impact model, which was implemented in an existing 3D rockfall trajectory model to calculate velocities of simulated boulders after a rebound on the slope. The first objective of this study was to assess the adequacy of the approach proposed. For this purpose, a full-scale experimental program made it possible to assess the predictive capacity of this tool. Comparisons between experimental and simulated results show very acceptable agreements. The second objective of the study was to evaluate the minimum amount of field data required to obtain accurate simulation results. The main advantages of the developed approach are the small number of parameters to be assessed in the field and the clear physical meaning of these parameters. Basically, only the mean size of the rocks covering the surface of the slope is required. This can be measured objectively in the field. The method developed does not work for boulders impacting fine soils. We believe, however, that a similar objective stochastic rebound model could be developed, based on a similar combination of numerical and laboratory experiments.

The stochastic feature of this new approach is an excellent basis for continuing integrating probabilistic information in rockfall hazard management. As reliable spatially distributed probabilistic information on rockfall trajectories is provided, such as the passing heights and kinetic energy distributions as well as the

passing frequencies for each position on a slope, the proposed approach offers a complete data set for positioning and designing rockfall protective structures as well as for hazard zoning.

References

Agliardi, F., Crosta, G.B., 2003. High resolution three-dimensional numerical modelling of rockfalls. International Journal of Rock Mechanics and Mining Sciences. 40, 455-471.

Azzoni, A., Rossi P.P., Drigo E., Giani G.P., Zaninetti A., 1992. In situ observations of rockfalls analysis parameters Proceedings of the sixth International Symposium of Landslides. Balkema, Rotterdam, The Netherlands, pp. 307-314.

Azzoni, A., Barbera, G.L., Zaninetti A., 1995. Analysis and prediction of rockfalls using a mathematical model. International Journal of Rock Mechanics and Mining Sciences. 32, 709-724.

Azzoni, A., De Freitas, M.H., 1995. Experimentally gained parameters, decisive for rock fall analysis. Rock Mechanics and Rock Engineering. 28 (2), 111-124.

Berger, F., Dorren, L.K.A., 2006. Objective comparison of rockfall models using real size experimental data. Disaster mitigation of debris flows, slope failures and landslides. Universal Academy Press Inc., Tokyo, Japan, pp. 245-252.

Bourrier, F., Nicot, F., Darve, F., 2007. Rockfall modelling: Numerical simulation of the impact of a particle on a coarse granular medium. Proc. 10th Int. Congr. on NUmerical MOdel in Geomechanics. Balkema, Rotterdam, The Netherlands, pp. 699-705.

Bourrier, F. 2008. Modélisation de l'impact d'un bloc rocheux sur un terrain naturel, application à la trajectographie des chutes de bloc. PhD thesis, Institut Polytechnique de Grenoble, France.

Bourrier, F., Nicot, F., Darve, F., 2008a. Physical processes within a 2D granular layer during an impact. Granular Matter. 10 (6), 415-437.

Bourrier, F., Eckert, N., Bellot, H., Heymann, A., Nicot, F., Darve, F., 2008b. Numerical modelling of physical processes involved during the impact of a rock on a coarse soil. Proc. 2nd Euro Med. Symp. On Advances in Geomaterial and Structures. Publisher, location of publisher, pp. 501-506.

515 Bozzolo, D., Pamini, R., 1986. Simulation of rock falls down a valley side. Acta Mechanica. 63, 113-130.
516 Chau, K. T., Wong, R.H.C., Lee, C. F., 1998. Rockfall Problems in Hong Kong and some new
517 Experimental Results for Coefficients of Restitution. International Journal of Rock Mechanics and
518 Mining Sciences. 35(4-5), 662-663.
519 Chau, K.T., Wong, R.H.C., Wu, J.J., 2002. Coefficient of restitution and rotational motions of rockfall
520 impacts. International Journal of Rock Mechanics and Mining Sciences. 39, 69-77.
521 Chau, K.T., Tang, Y.F., Wong, R.H.C., 2004. GIS based rockfall hazard map for Hong Kong.
522 International Journal of Rock Mechanics and Mining Sciences. 41(1), 846-851.
523 Cruden, D.M., Varnes, D.J., 1996. Landslides types and processes : Chapter 3. In: Turner, A.K., Schuster,
524 R.L., (Eds.), Landslides: Investigation and Mitigation. Transportation research board, Special report
525 247, pp. 36-71.
526 Descoeudres, F., 1997. Aspects géomécaniques des instabilités de falaises rocheuses et des chutes de
527 blocs. Publications de la société suisse de Mécanique des Sols et des Roches. 135, 3-11.
528 Dorren, L.K.A., 2003. A review of rockfall mechanics and modelling approaches. Progress in Physical
529 Geography. 27 (1), 69-87.
530 Dorren, L.K.A., Berger, F., Le Hir, C., Mermin, E., Tardif, P., 2005. Mechanisms, effects and
531 management implications of rockfall in forests. Forest Ecology and Management. 215(1-3), 183-195.
532 Dorren, L.K.A., Berger, F., Putters, U.S., 2006. Real size experiments and 3D simulation of rockfall on
533 forested and non-forested slopes. Natural Hazards and Earth System Sciences. 6, 145-153.
534 Dudt, J.P., Heidenreich, B., 2001. Treatment of the uncertainty in a three-dimensional numerical
535 simulation model of rockfalls. International Conference on Landslides. pp. 507-514.
536 Evans, S.G., Hungr, O., 1993. The assessment of rockfall hazard at the base of talus slopes. Canadian
537 Geotechnical Journal. 30, 620-636.
538 Frattini, P., Crosta, G.B., Carrara, A., Agliardi, F., 2008. Assessment of rockfall susceptibility by
539 integrating statistical and physically-based approaches. Geomorphology. 94 (3-4), 419-437.

Guzzetti, F., Crosta, G., Detti, R., Agliardi F., 2002. STONE: a computer program for the three dimensional simulation of rock-falls. Computer & Geosciences. 28, 1079-1093.

Heidenreich, B., 2004. Small- and half-scale experimental studies of rockfall impacts on sandy slopes. PhD Thesis, Ecole Polytechnique Fédérale de Lausanne, Swiss.

Interreg IIc., 2001. Prévention des mouvements de versants et des instabilités de falaise - Confrontation des méthodes d'étude des éboulements rocheux dans l'arc alpin. Final report, Interreg IIc Program Méditerranée occidentale et Alpes Latines.

Jaboyedoff, M., Dudt, J.P., Labiouse, V., 2005. An attempt to refine rockfall zoning based on kinetic energy, frequency and fragmentation degree. Natural Hazards and Earth System Sciences. 5, 621-632.

Kobayashi, Y., Harp, E.L., Kagawa, T., 1990. Simulation of rockfalls triggered by earthquakes. Rock Mechanics and Rock Engineering. 23, 1-20.

Nicot, F., Cambou, B., Mazzoleni, G., 2001. From a constitutive modelling of metallic rings to the design of rockfall restraining nets. International Journal for Numerical and Analytical Methods in Geomechanics. 25, 49–70.

Nicot, F., Gotteland, P., Bertrand, D., Lambert, S., 2007. Multiscale approach to geo-composite cellular structures subjected to rock impacts. International Journal for Numerical and Analytical Methods in Geomechanics. 31, 1477-1515.

Paronuzzi, P., 1989. Probabilistic approach for design optimization of rockfall protective barriers. Quarterly Journal of Engineering Geology and Hydrogeology. 22, 175-183.

Peila, D., Pelizza, S., Sasssudelli, F., 1998. Evaluation of behaviour of rockfall restraining nets by full scale tests. Rock Mechanics Rock Engineering. 31 (1), 1-24.

Pfeiffer, T.J., Bowen, T.D., 1989. Computer simulations of rockfalls. Bulletin of the Association of Engineering Geology. 26, 135-146.

Raetzo, H., Lateltin, O., Bollinger, D., Tripet, J., 2002. Hazard assessment in Switzerland – Codes of practice for mass movements. Bulletin of engineering Geology and the Environement. 61(3), 263-268.

565 Scioldo, G., 2006. User guide ISOMAP & ROTOMAP - 3D surface modelling and rockfall analysis.
566 Geo&Soft International.
567 Selby, M. J., 1993. Hillslope materials and processes. Oxford University Press, Oxford.
568 Ushiro, T., Shinohara, S., Tanida, K., Yagi, N., 2000. A study on the motion of rockfalls on Slopes.
569 Proceedings of the 5th Symposium on Impact Problems in Civil Engineering. pp. 91-96.
570 Varnes, D.J., 1978. Slope movement types and processes. In: Schuster, R.L., Krizek, R.J., (Eds.),
571 Landslides, analysis and control. Transportation research board, Special report 176, pp. 11-33.
572 Weber, D., and Englund, E., 1992. Evaluation and comparison of spatial interpolators. Mathematical
573 Geology. 24, 381-391.
574 Whalley, W.B., 1984. Rockfalls. In: D. Brunsden, D., Prior, D.B. (Eds), Slope instability. John Wiley and
575 Sons, New York, pp. 217-256.
576 Wu, S.S., 1985. Rockfall evaluation by computer simulation. Transportation Research Record. 1031, 1-5.
577

578 **List of figures**

579 Fig. 1. A) Google Earth image of the area around Grenoble (France) and the location of the study area; B)
580 location of the study area in the valley of the Eau d'Olle (Google Earth); C) picture of the study area from
581 a facing slope; D) map of the study area with an indication of 14 homogenous zones with different types
582 of surface roughness (dense fine dots = fine material; large dots = rough talus material, see Section 3.4),
583 the position of the two evaluation lines (EL1 and EL2), the release point and the 5 cameras.
584 Fig. 2. Experimental boulder volume distribution.
585 Fig. 3. Sequence of movie images.
586 Fig. 4. Example of A) the simulated rockfall trajectory plotted on a contour line map (*x*-*y* plan view); B)
587 the trajectory in the *x*–*z* plane (*z*-axis corresponds to the vertical direction); and C) the simulated velocity
588 versus the *x* coordinate.

589 Fig. 5. Definitions of outgoing (V_t^{out}, V_n^{out}, and ω^{out}) and incident (V_t^{in}, V_n^{in}, and ω^{in}) velocity components
590 used in the stochastic impact model and of the deviation angle δ characterising changes in boulder fall
591 direction due to the rebound.
592 Fig. 6. Predictions of the mean values of the R_t and R_n coefficients versus the incident angle α^{in} using the
593 stochastic impact model.
594 Fig. 7. Plan view (x–y plane) illustrating the principle used for calculating the fall direction after rebound.
595 The deviation of the boulder from its direction before rebound is only allowed towards the aspect.
596 Fig. 8. Distribution of the velocities, passing heights, and translational kinetic energy for observed and
597 simulated trajectories for EL1 scaled to the observed values for both methods A ("size classes") and B
598 ("mean size").
599 Fig. 9. Percentage of passing boulder versus distance from the release point for the experiments, method
600 A ("size classes") and method B ("mean size").
601 Fig. 10. Map of the simulated pass frequencies for methods A ("size classes") and B ("mean size") and
602 the observed stopping points (white dots).
603 Fig. 11. Distribution of the simulated rotational kinetic energy compared with the total kinetic energy for
604 EL1 and EL2 using method B ("mean size").
605 Fig. 12. Distribution of the simulated tangential incident energy E_t^{in} compared with the total incident
606 energy E_{tot}^{in} for all the simulated rebounds using method B ("mean size").
607 Fig. 13. Distributions of the incidence angle α^{in} over all the simulations using method B ("mean size").
608
609 Fig. 14. Distribution of the tangential and normal restitution coefficients R_t and R_n over all simulations
610 using method B ("mean size").
611 Fig. 15. Hillshade of the DEM showing the study site downslope from camera 5. The white dotted circle
612 outlines the imperfect digital representation of the terrain. Black arrow 1 shows the main simulated

613 trajectory. Black arrow 2 indicates the second main trajectory and its deviation due the artefact in the
614 DEM. The small grey circles represent the stopping positions of the experimental boulders.
615 Fig. 16. A typical field situation in Zone 3, where the surface material should be characterised by size
616 classes method.
617

618 **List of tables**

619 Table 1. For method A, the surface material size is defined using three roughness classes Rg_{70}, Rg_{20}, Rg_{10}
620 and, for method B, the surface material size is defined using the parameter R_m.
621 Table 2. Results after 10,000 simulation runs for both methods A (“size classes”) and B (“mean size”).
622 Table 3. Relative errors (RE) compared to observations after 10,000 simulation runs for both methods A
623 (“size classes”) and B (“mean size”).
624 Table 4. Kolmogorov-Smirnov tests (KS tests) compared to experimental distributions after 10,000
625 simulation runs for both methods A (“size classes”) and B (“mean size”).

626 Fig. 1.

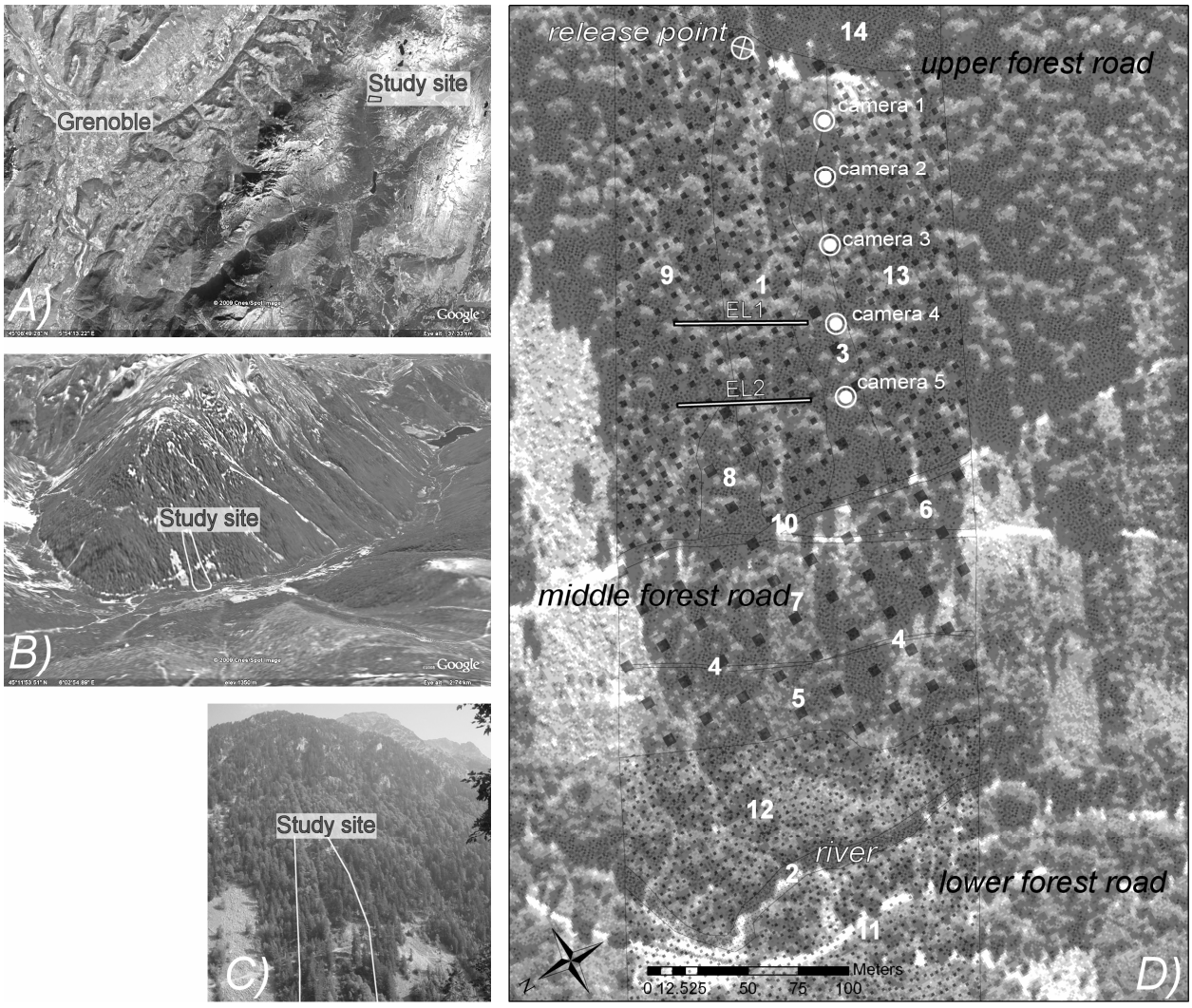
Grenoble
Study site
A)
Study site
B)
Study site
C)
release point
14
upper forest road
camera 1
camera 2
camera 3
9
1
13
EL1
camera 4
3
EL2
camera 5
8
10
6
middle forest road
7
4
4
5
12
river
2
lower forest road
11
Meters
0 12.525 50 75 100
D)

627

628 Fig. 2.

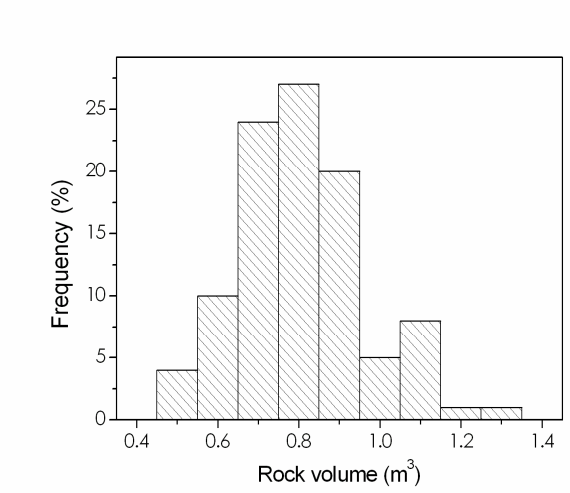

629

630 Fig. 3.

631 

632 Fig. 4.

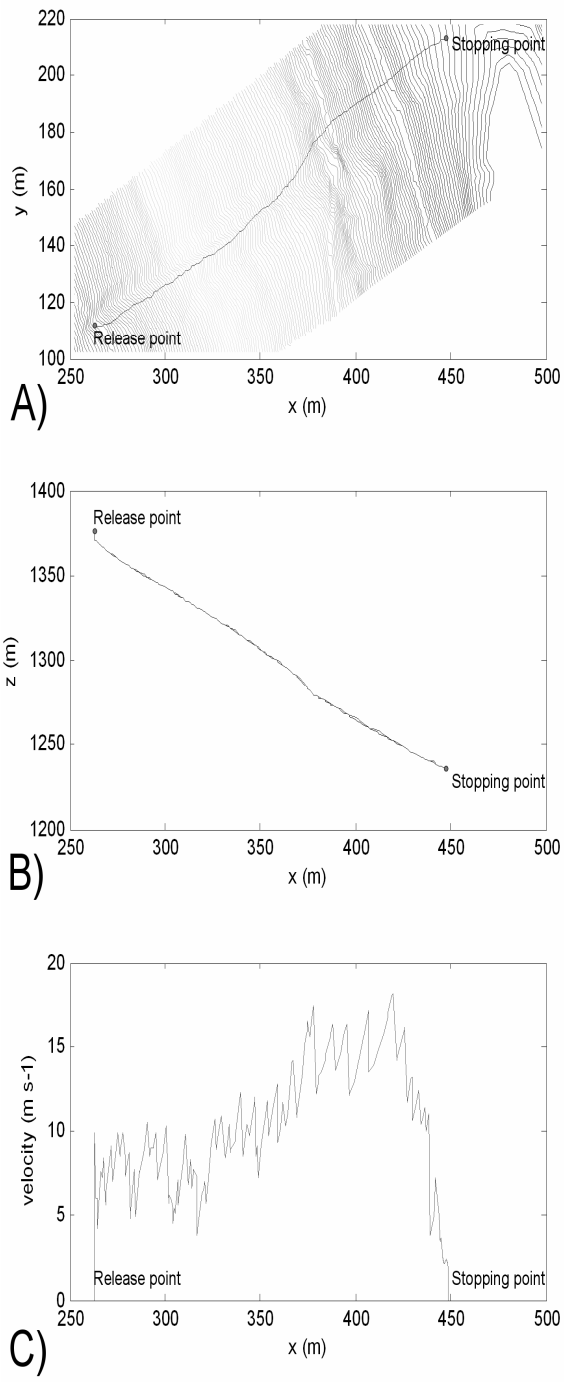
Stopping point
Release point
y (m)
x (m)
A)
Release point
Stopping point
z (m)
x (m)
B)
velocity (m s-1)
Release point
Stopping point
x (m)
C)

633

634 Fig. 5.

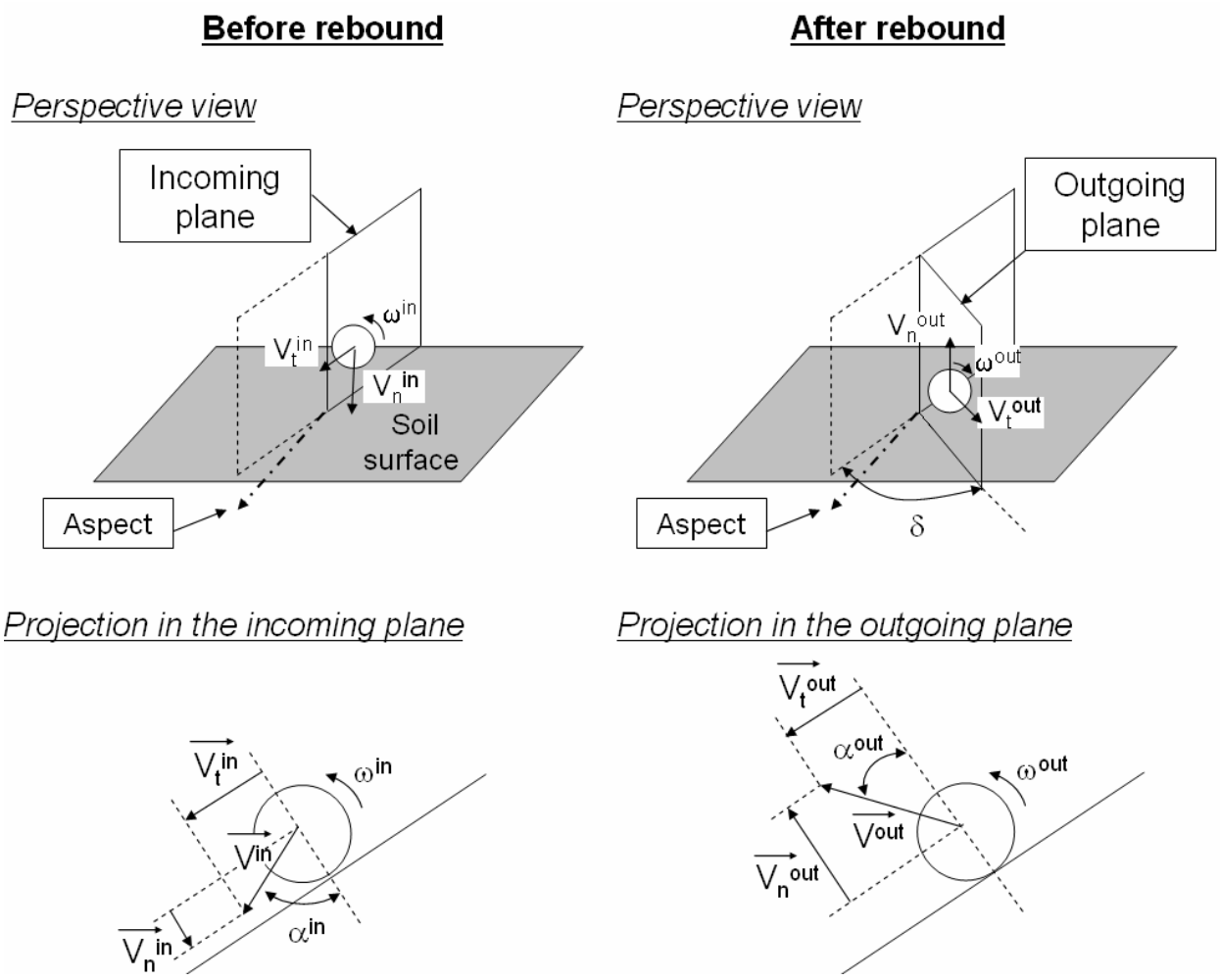
Before rebound
After rebound
Perspective view
Perspective view
Incoming plane
Outgoing plane
ω^{in}
V_t^{in}
V_n^{in}
Soil surface
Aspect
V_n^{out}
ω^{out}
V_t^{out}
Aspect
δ
Projection in the incoming plane
Projection in the outgoing plane
$\overrightarrow{V_t^{in}}$
ω^{in}
$\overrightarrow{V^{in}}$
α^{in}
$\overrightarrow{V_n^{in}}$
$\overrightarrow{V_t^{out}}$
α^{out}
ω^{out}
$\overrightarrow{V^{out}}$
$\overrightarrow{V_n^{out}}$

635

636 Fig. 6.

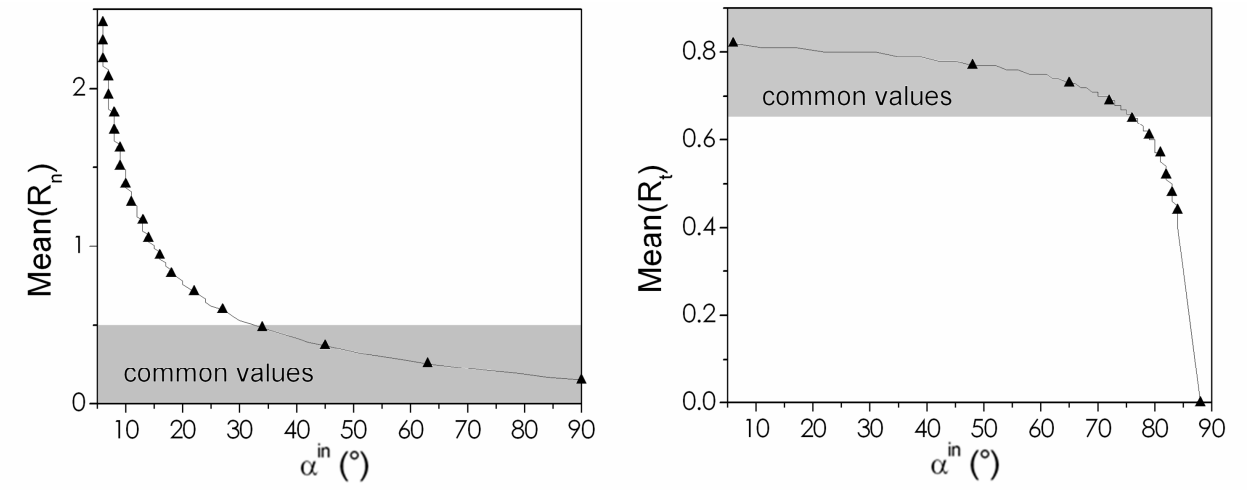

637

638 Fig. 7.

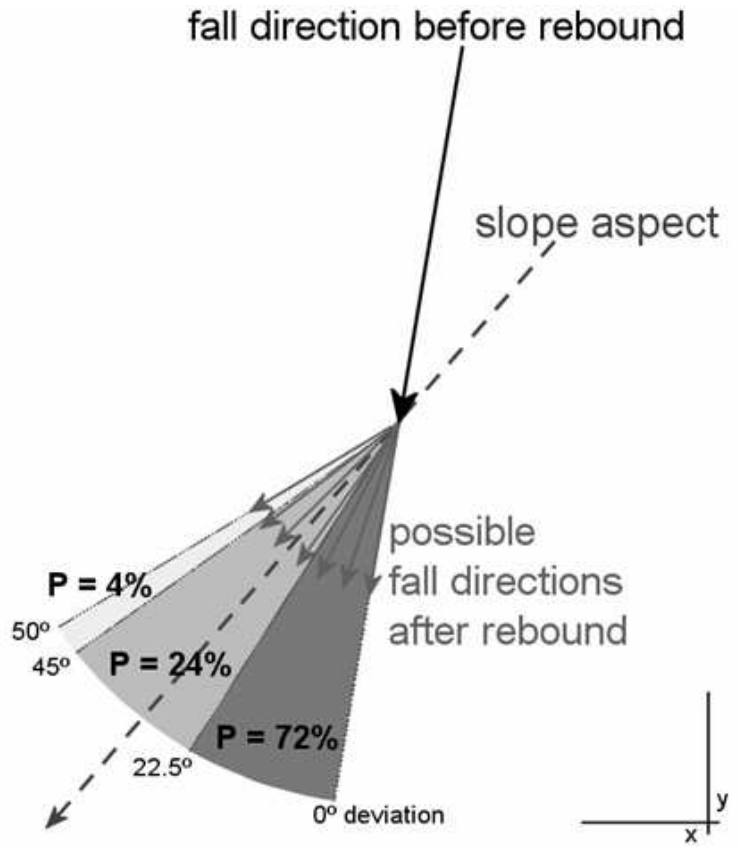
fall direction before rebound
slope aspect
possible
fall directions
after rebound
P = 4%
50°
45°
P = 24%
P = 72%
22.5°
0° deviation
y
x

639

640 Fig. 8.

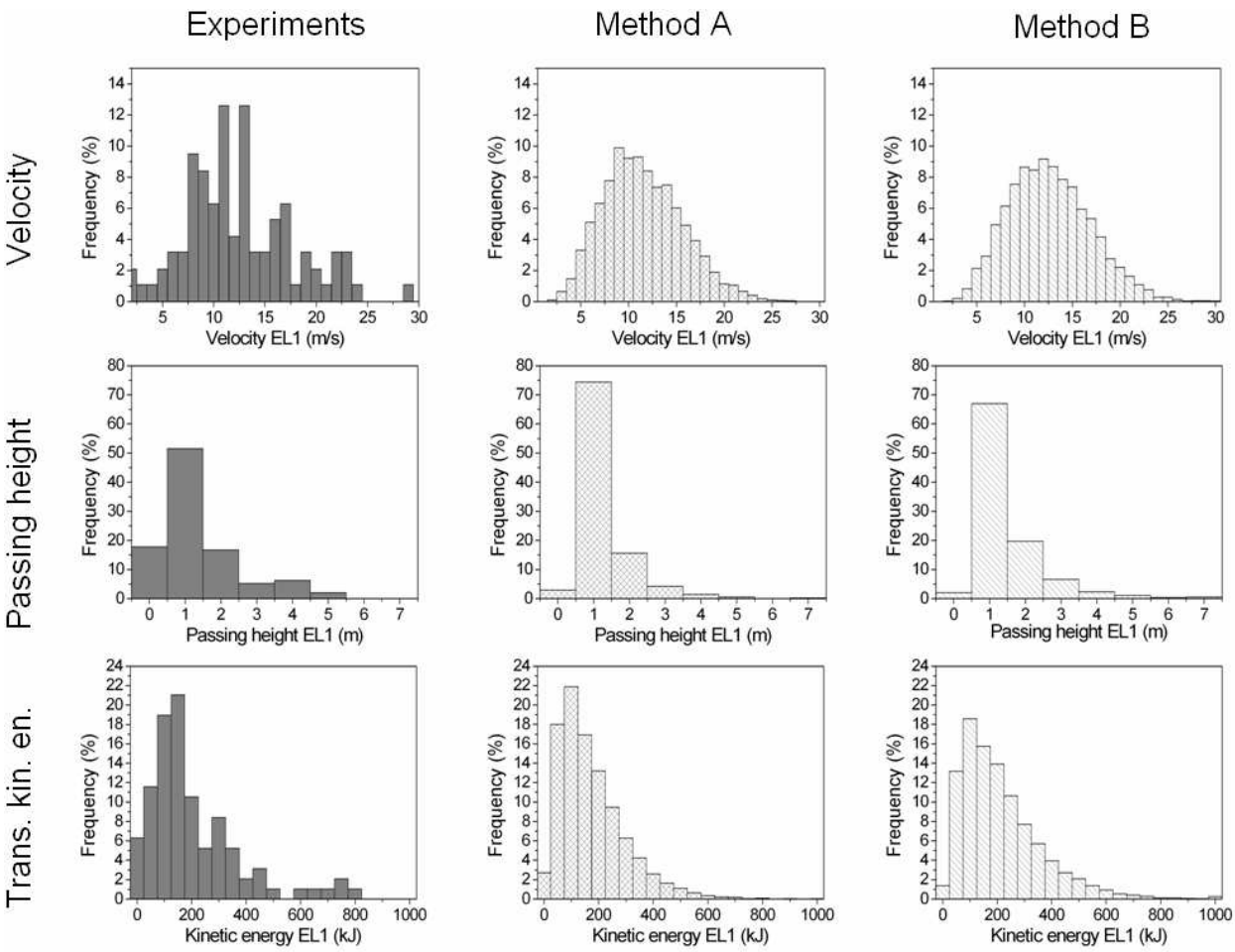
Experiments
Method A
Method B
Velocity
Passing height
Trans. kin. en.
Frequency (%)
Velocity EL1 (m/s)
Passing height EL1 (m)
Kinetic energy EL1 (kJ)

641

642 Fig. 9.

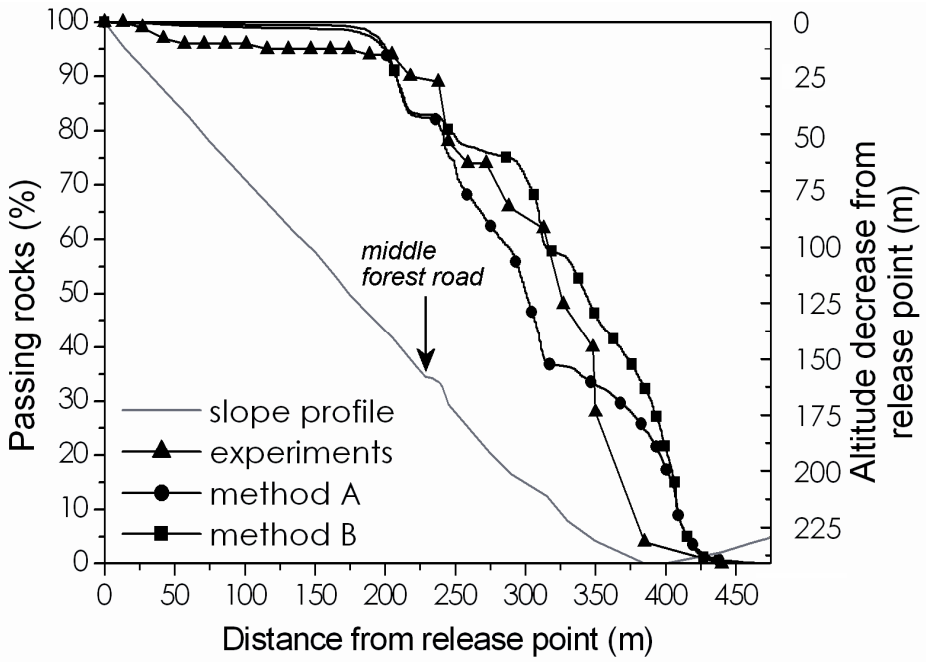
Passing rocks (%)
Altitude decrease from release point (m)
Distance from release point (m)
middle forest road
slope profile
experiments
method A
method B
0
10
20
30
40
50
60
70
80
90
100
0
25
50
75
100
125
150
175
200
225
0
50
100
150
200
250
300
350
400
450

643

644 Fig. 10.

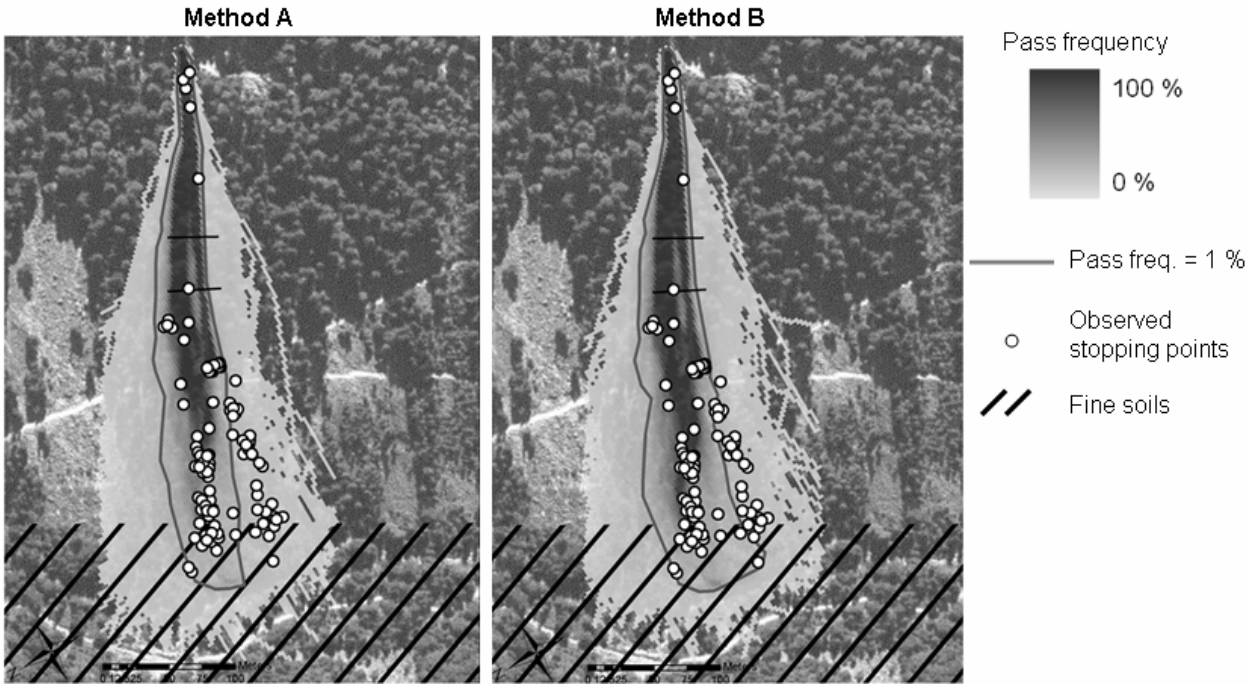

645

646 Fig. 11.

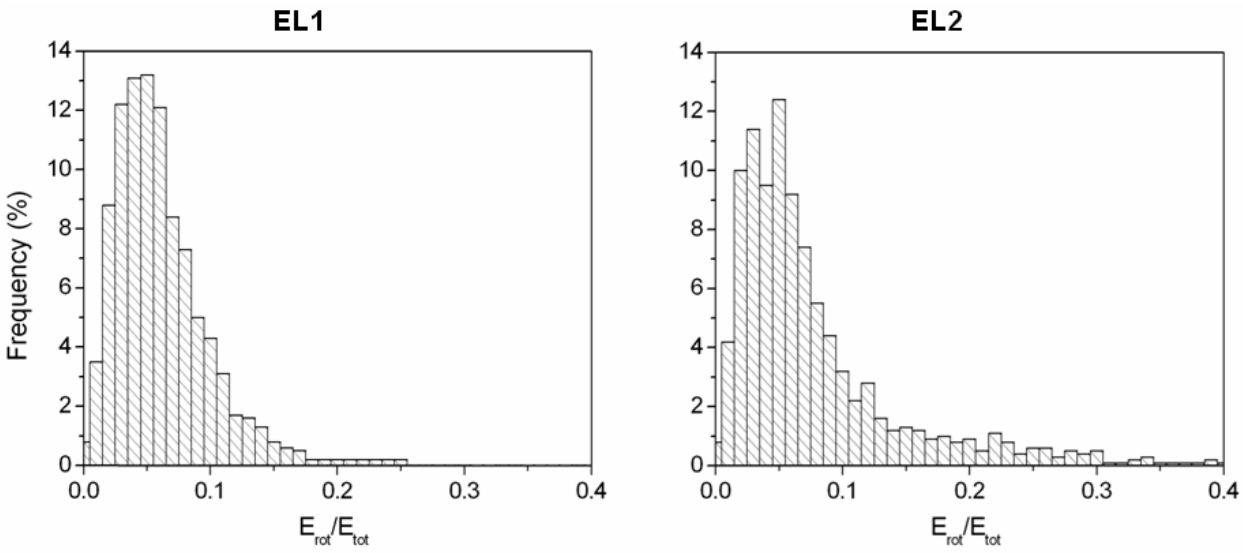

647

648 Fig. 12.

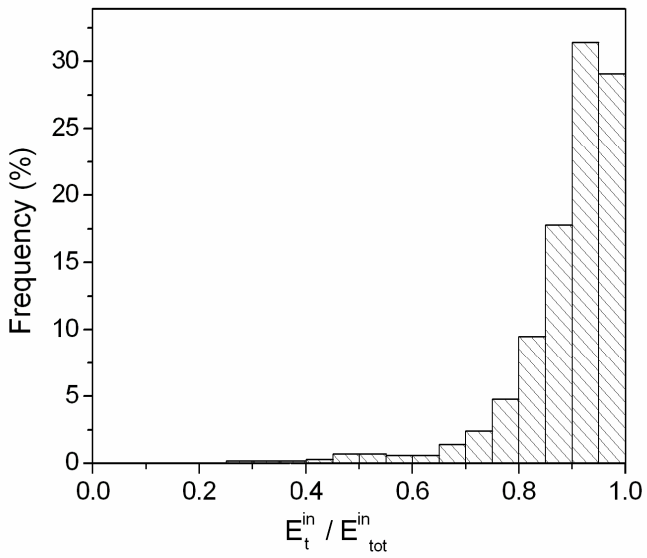

649

650 Fig. 13.

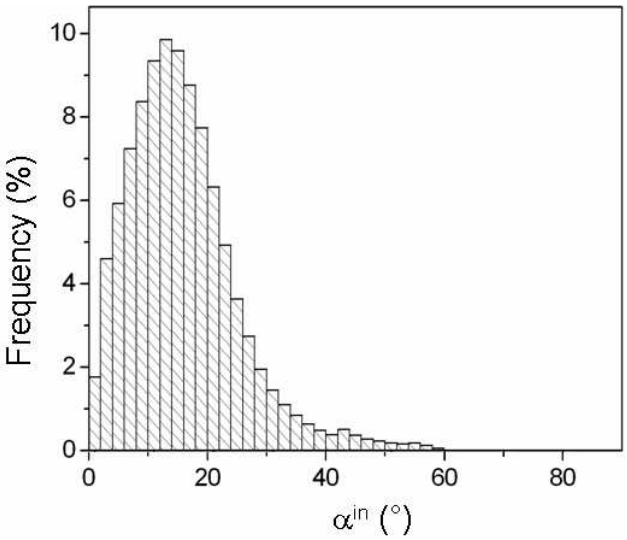

651

652 Fig. 14.

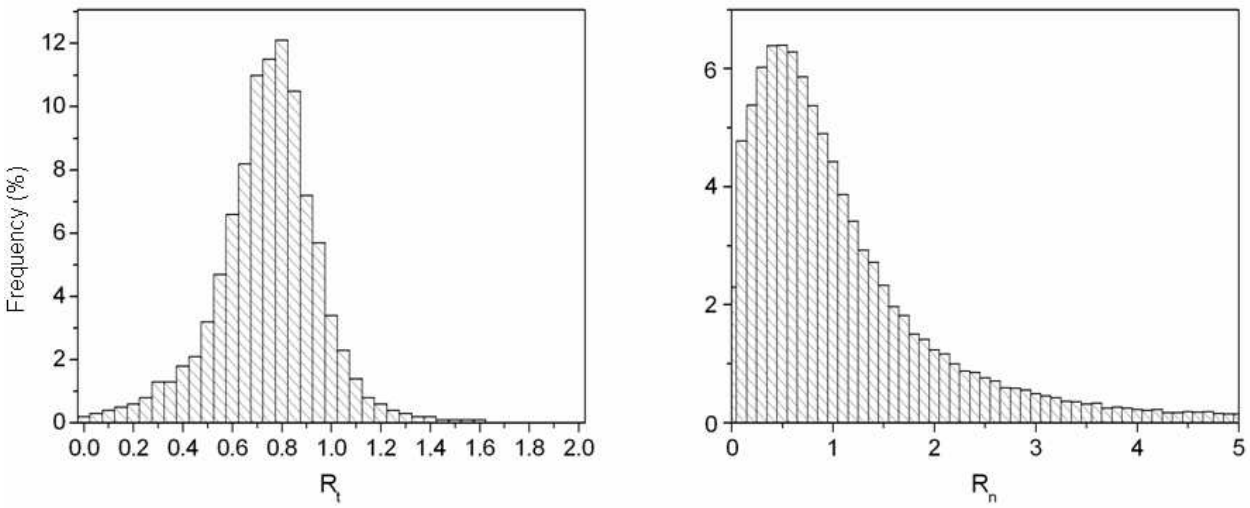

653

654 Fig. 15.

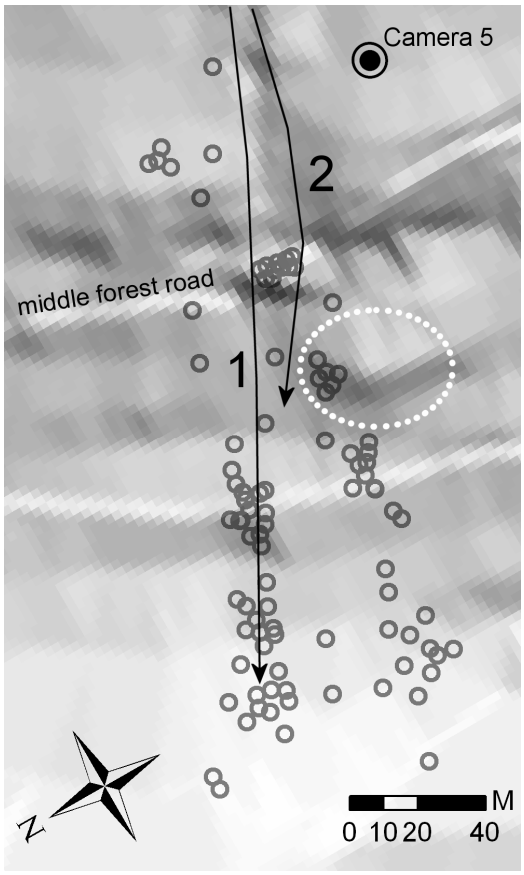

655

Fig. 16.

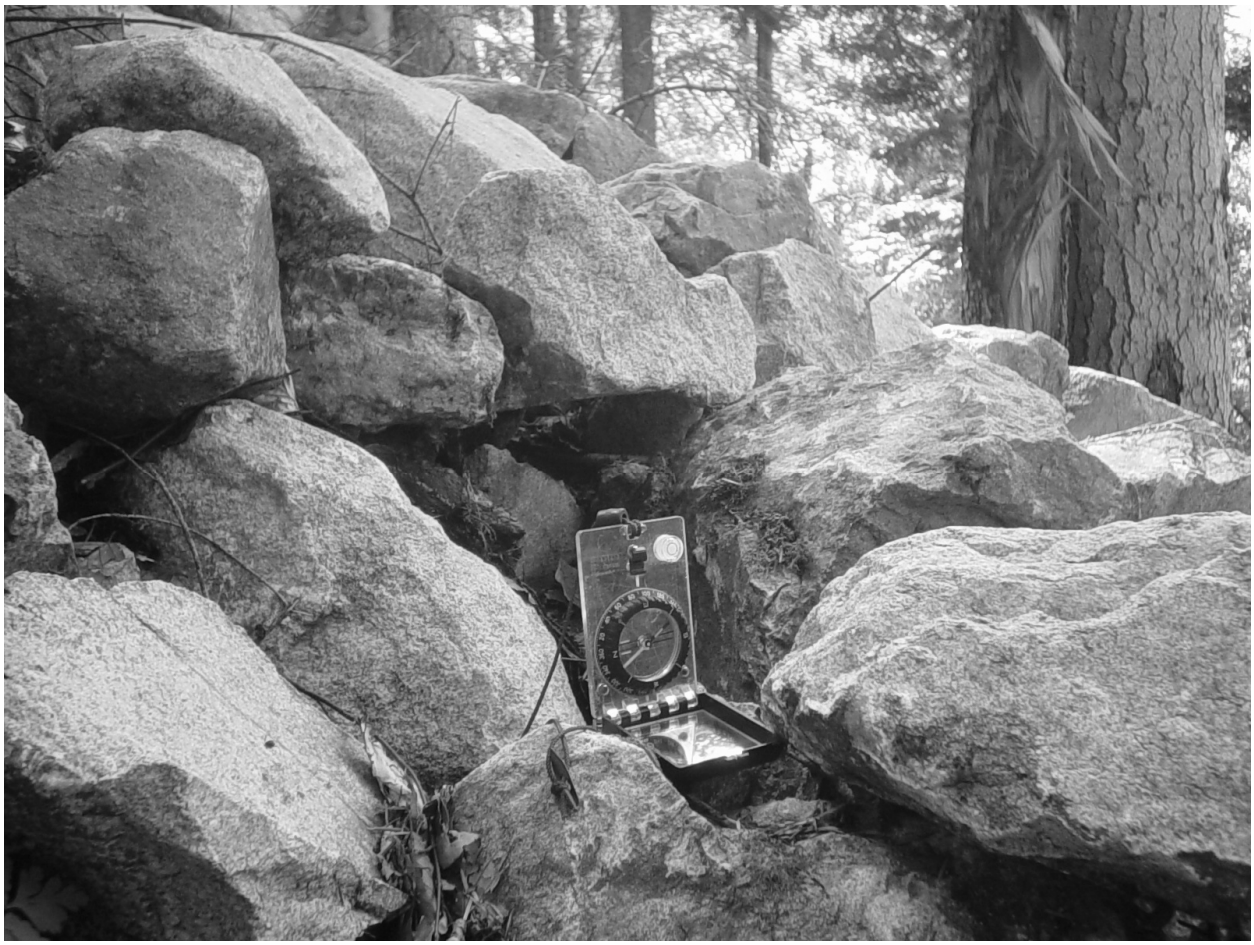

658 Table 1.

Zone	Rg_{70} (m)	Rg_{20} (m)	Rg_{10} (m)	R_m (m)	Description
1	0.20	0.15	0.07	0.10	Inside the avalanche channel
2	Inf	Inf	Inf	Inf	River
3	0.30	0.10	0.45	0.18	Zone covered with talus alongside the channel
4	0.50	0.30	0.10	0.25	Old road on talus slope, covered with single blocks
5	0.40	0.20	0.10	0.25	Talus slope downslope of middle forest road
6	0.50	0.25	0.75	0.25	Rough talus slope downslope of middle forest road
7	0.50	0.28	0.90	0.25	Roughest part of the talus slope downslope of middle forest road
8	0.40	0.25	0.50	0.25	Small block accumulation
9	0.20	0.05	0.10	0.10	North-east forested part of talus slope
10	0.50	0.30	0.10	0.10	Irregular forest road on talus slope
11	0.05	0.05	0.05	0.05	Soils in valley bottom
12	0.02	0.05	0.10	0.03	Fine soils in valley bottom
13	0.25	0.15	0.10	0.10	South-west forested part of talus slope
14	0.10	0.20	0.30	0.10	Upper forest road

659 Table2.

	Velocity (m. s^{-1})			Passing height (m)			Trans. kin. en. (kJ)		
	Mean	**Std. Dev.**	**Max.**	**Mean**	**Std. Dev.**	**Max.**	**Mean**	**Std. Dev.**	**Max.**
EL1[a] observed	12.5	5.2	28.1	1.4	1.1	5.0	205	169	786
EL1 method A	11.5	4.2	27.7	1.2	0.9	10.4	175	126	1081
EL1 method B	12.7	4.3	30.3	1.4	1.0	11.0	213	152	1332
EL2 observed	13.8	5.5	28.9	1.6	1.4	6.2	245	196	958
EL2 method A	10.9	4.7	29.6	1.2	1.0	15.5	167	139	1174
EL2 method B	12.1	5.1	31.8	1.4	1.1	12.7	207	173	1575

660 [a] EL = Evaluation line.

661

662 Table 3.

	RE velocity (%)			RE passing height (%)			RE Trans. kin. en. (%)		
	Mean	**Std. Dev.**	**Max.**	**Mean**	**Std. Dev.**	**Max.**	**Mean**	**Std. Dev.**	**Max.**
EL1 method A	−8	−19	−1	−14	−18	108	−15	−25	38
EL1 method B	2	−17	8	0	−9	120	4	−10	69
EL2 method A	−21	−15	2	−25	−29	150	−32	−29	23
EL2 method B	−12	−7	10	−13	−21	105	−16	−12	64

663 Table 4.

	Velocity		**Passing height**		**Trans. kin. en.**	
	KS test 0: not rejected 1: rejected	**P-value**	**KS test 0: not rejected 1: rejected**	**P-value**	**KS test 0: not rejected 1: rejected**	**P-value**
EL1 method A	0	0.2225	1	0.0385	0	0.1772
EL1 method B	0	0.2172	0	0.0570	0	0.1421
EL2 method A	1	0.0033	1	0.0224	1	0.0223
EL2 method B	0	0.1022	1	0.0366	0	0.2911

664